Variation in the Pedersen Conductance near Jupiter's Main Emission Aurora: Comparison of Hubble Space Telescope and Galileo Measurements

M. J. Rutala[1,2], J. T. Clarke[2], M. F. Vogt[2], and J. D. Nichols[3]

[1]School of Cosmic Physics, DIAS Dunsink Observatory, Dublin Institute for Advanced Studies, Dublin 15, Ireland
[2]Center for Space Physics, Boston University, Boston MA
[2]Department of Physics and Astronomy, University of Leicester, Leicester UK

Key Points:

- The effective ionospheric Pedersen conductance in Jupiter's main emission auroral region is derived from remote and in-situ measurements.
- Field-aligned auroral currents of ~ 10 MA rad^{-1} and effective Pedersen conductances of ~ 0.14 mho are derived, consistent with past research.
- The effective Pedersen conductance varies primarily in magnetic local time, and may explain the enigmatic motions of some auroral forms.

Corresponding author: M. J. Rutala, `mrutala@bu.edu`

Abstract

We present the first large-scale statistical survey of the Jovian main emission (ME) to map auroral properties from their ionospheric locations out into the equatorial plane of the magnetosphere, where they are compared directly to in-situ spacecraft measurements. We use magnetosphere-ionosphere (MI) coupling theory to calculate currents from the auroral brightness as measured with the Hubble Space Telescope and from plasma flow speeds measured in-situ with the *Galileo* spacecraft. The effective Pedersen conductance of the ionosphere (Σ_P^*) remains a free parameter in this comparison. We first show that the field-aligned currents per radian of azimuth calculated from the auroral observations, found to be $I_{||} = 9.54_{-6.35}^{+11.5}$ MA rad^{-1} and $I_{||} = 10.64_{-6.11}^{+11.1}$ MA rad^{-1} in the north and south, respectively, are consistent with previous results. Then, we calculate the Pedersen conductance from the combined datasets, and find it ranges from $0.02 < \Sigma_P^* < 2.26$ mho overall with averages of $0.14_{-0.08}^{+0.31}$ mho in the north and $0.14_{-0.09}^{+0.26}$ mho in the south. Taking the currents and effective Pedersen conductance together, we find that the average ME intensity and plasma flow speed in the middle magnetosphere (10-30 R_J) are broadly consistent with one another under MI coupling theory. We find evidence for peaks in the distribution of Σ_P^* near 7, 12, and 14 hours magnetic local time (MLT). This variation in Pedersen conductance with MLT may indicate the importance of conductance in modulating MLT- and local-time-asymmetries in the ME, including the apparent sub-corotation of some auroral features within the ME.

Plain Language Summary

The brightest part of Jupiter's aurorae– the main emission– forms arcs of sheet-like lights surrounding both magnetic poles, similar to the Earth's aurorae. At both planets, these lights are caused by charged particles flowing into the planet's atmosphere, where they collide with gases and glow. At Jupiter, these particles are electrons which flow in electrical currents connecting the planet to the charged-particle-filled space surrounding it. Here, we use Hubble Space Telescope images of Jupiter's aurorae spanning a decade to build up an average picture of the brightness and location of this main emission. The brightness is related to the energy of the electrons, which in turn is related to the strength of electrical currents flowing near the planet. We then use particle measurements made by the Galileo spacecraft in orbit around Jupiter to make an average picture of these particle's as they move around Jupiter. These speeds are related to the same electrical currents, but include an electrical conductivity term describing how easily currents flow through Jupiter's auroral atmosphere. We combine all these measurements to calculate the conductivity, and present results which are consistent with expectations but which fluctuate more quickly than expected in parts of the main emission.

1 Introduction

Jupiter's ultraviolet (UV) auroral main emission (ME), typically the most powerful component of the planet's large-scale auroral regions, takes the form of a partially-closed oval of auroral emission surrounding each of the planet's magnetic poles. The Jovian aurorae are detectable at all local times (LT) including on the planet's dayside(Clarke et al., 2004; Bonfond et al., 2017), where they are significantly brighter than Jupiter's surface UV emission (Gustin et al., 2012) and can thus be observed routinely with the Hubble Space Telescope (HST). In the southern hemisphere, the ME forms a nearly circular curtain of light; however, the presence of multiple significant non-dipolar magnetic field components in the northern hemisphere complicates the structure, resulting in a characteristic 'kidney bean' shape (Grodent et al., 2008; Connerney et al., 2022), as shown by the HST observation and statistically-averaged reference main oval ('statistical main oval', or SMO) in Figure 1a.

The ME has historically been thought to originate from the magnetosphere-ionosphere (MI) coupling currents flowing in the Jovian middle magnetosphere, radially outward in the equatorial plasma disc, equatorward in the ionosphere, and along magnetic field lines between (Hill, 2001; Cowley & Bunce, 2001; Nichols & Cowley, 2003, 2004, 2005; Ray et al., 2010, 2014; Smith & Aylward, 2009; Tao et al., 2009). This current system arises from the azimuthal distortion (or 'bendback') of the field caused by the planet's reservoir of angular momentum opposing the decrease in angular velocity of flux tubes laden with Iogenic plasma as they diffuse radially outward . In the absence of torques, these diffusing flux tubes would tend to conserve angular momentum, resulting in a decrease in the angular velocity proportional to r^{-2}. The resultant lag in the flux tubes corresponds to an azimuthal bendback in the magnetic field structure and thus a loop of field-aligned current which acts to partially enforce the corotation of the plasma composing the plasma disk by exerting a $\mathbf{J} \times \mathbf{B}$ force in the direction of corotation. The strongest field-aligned currents occur near where rigid corotation breaks down (Hill, 1979; Nichols & Cowley, 2004) . The ME current system is characterized primarily by the rapid rotation and strength of Jupiter's magnetic field, rather than by solar influence as is the case in the Earth's own magnetosphere and auroral ovals (Cowley & Bunce, 2001; Southwood & Kivelson, 2001) , though solar wind influence is not completely absent (Kita et al., 2019; Nichols et al., 2017). These MI-coupling currents and the associated ME ovals are thus always present, owing to the continuous production of Iogenic plasma and diffusion of this plasma outward through the magnetosphere.
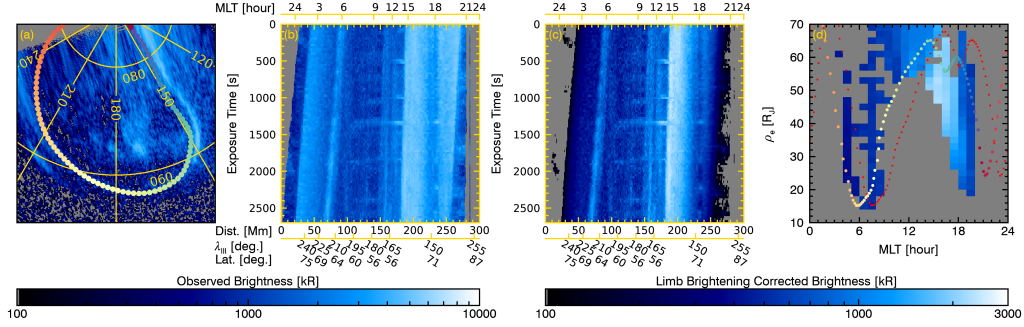
The production and diffusion of Iogenic plasma is not constant and the Jovian magnetosphere is varies in System III (SIII) magnetic longitude (λ_{III}), local time (LT), and magnetic local time (MLT). This results in various asymmetries in the brightness, shape, distribution, and dynamics of auroral forms within the ME oval. The southern ME is brighter on average than the northern (Gérard et al., 2013) and the dusk side of the ME is brighter on average than dawn, an effect which is amplified in the brighter southern hemisphere (Bonfond et al., 2015). On occasions where the dawn side is brighter than dusk, an exceptionally bright auroral feature– a dawn storm, perhaps– is typically located on the dawn ME (Gérard, Grodent, et al., 1994; Bonfond et al., 2021; Rutala et al., 2022). While the locations of the ME remain fixed in SIII longitude and latitude (Clarke et al., 2004; Gérard, Dols, et al., 1994; Grodent et al., 2003), auroral features on the ME may subcorotate, lagging behind the rigid corotation rate of the planet. Subcorotation occurs more often in the dawn sector than the noon and dusk sectors (Rutala et al., 2022), an effect which appears to be separate from the appearance of bright dawn storms. Additional subcorotating auroral forms, the ME auroral discontinuity (Radioti et al., 2008) and small-scale brightening (Palmaerts et al., 2014) are observed localized near noon. The dusk side of the ME as viewed from the Earth is typically wider and more diffuse than near dawn (Gérard, Dols, et al., 1994); this asymmetry is larger in the northern hemisphere, where the northern magnetic anomaly is typically located in remote observations (Grodent et al., 2008). This asymmetry was originally considered to be a variation in local time (Caldwell et al., 1992), before improved HST observations made it appear to be a variation in SIII longitude (Gérard, Dols, et al., 1994). Recent *Juno* observations of the ME oval morphology indicate that this asymmetry may vary in a more complex way, dependent on both local time and SIII longitude (Greathouse et al., 2021).

These phenomena have generally been thought to arise from deviations from the ideal axisymmetric MI-coupling theory previously discussed. However, predictions of this theory are not always in accordance with observations, raising the possibility that the MI-coupling theory itself only partially describes the generation of the ME oval at Jupiter (Bonfond et al., 2020). Mean field-aligned MI-coupling currents of 58 MA and 24 MA in the southern and northern ME regions, respectively, have been derived from *Juno* measurements, reflecting the observed north-south brightness asymmetry of the ME ovals (Kotsiaros et al., 2019). These currents appear in primarily longitudinal, though variable, sheets in keeping with the schematic picture of MI coupling theory. Further *Juno*

measurements have found that the field lines associated with ME aurorae host precipitating electrons, as required to drive field-aligned currents, along with bi-directional electron distributions (Mauk et al., 2017, 2018), suggesting that additional auroral emission zones, co-located or nearly co-located with the ME, may be driven by acceleration processes other than field-aligned potentials (Mauk et al., 2020). The measured bi-directional electron distributions may, however, be a secondary effect, driven by the flow of intense field-aligned currents (Nichols & Cowley, 2022). The equatorial radial currents derived from *Juno* magnetometer measurements are highly correlated with simultaneous HST observations of the dawnside ME auroral intensity (Nichols & Cowley, 2022). On large scales, the MI-coupling theory still explains the bulk of the observed variation in ME auroral brightness, including during short-term enhancements (Nichols et al., 2020).

A further discrepancy between the modeled and observed auroral MI-coupling system at Jupiter lies in the auroral brightness asymmetry across the dayside ME. While the dusk side of the ME oval is typically observed to be brighter than the dawn side (Bonfond et al., 2015), models predict that this asymmetry should be reversed owing to the larger field bend-back in the dawn sector (Ray et al., 2014). Field bend-back is strongly correlated with ME auroral brightness, particularly near dawn (Nichols & Cowley, 2022). Field bend-back is caused by angular plasma flow speeds in the middle magnetosphere slower than the rotation rate of the planet, or subcorotation relative to the planet's rotation, so in considering only the quasi-steady-state MI coupling current system, an anticorrelation between the degree of field bend-back and plasma angular velocity is expected (Bonfond et al., 2020). A partial ring current, spanning the nightside middle magnetosphere with a source near dusk and a sink near dawn (Walker & Ogino, 2003) may ease this tension if the ring current closes along field-aligned currents, decreasing the effective field-aligned currents near dawn and increasing them near dusk (Bonfond et al., 2015). On top of this effect, careful consideration is required to relate instantaneous, in-situ measurements of plasma velocity to the measurement of magnetic field bend-back in a dynamic region of the magnetosphere such as the dawn sector. The anticorrelation between field bend-back and plasma velocity is only maintained in the quasi-steady-state scenario. If magnetospheric plasma near dawn is rapidly accelerated, the measured plasma velocity may be high despite large degrees of field bend-back, as the plasma and field lines have yet to "catch up" to corotational velocity. This scenario matches observations of both the plasma (Krupp et al., 2001; Bagenal et al., 2016) and the magnetic field (Khurana & Schwarzl, 2005) near dawn. Such a sudden acceleration of the middle magnetospheric plasma may be driven by an equally sudden increase in the conductance of the MI-coupling circuit, as is the case near the dawn terminator where the previously-unlit ionosphere is re-photoionized by solar extreme ultraviolet (EUV) light (Tao et al., 2010). This scenario has been suggested to explain the apparent subcorotation of some auroral forms relative relative to the SMO in the dawn sector (Rutala et al., 2022), and will be explored here in more detail.

Here, we present the first large-scale statistical survey of the typical HST-observed ME brightness, spanning more than 10 years and 200 cumulative hours of exposure time. The ME brightness is mapped from the polar ionosphere out into the magnetospheric equatorial plane and averaged in bins defined by MLT, equatorial radial distance (ρ_e), and the solar central meridian longitude (solar CML), so that variations relative to MLT and λ_{III} can be differentiated. From these binned values, the associated maximum field-aligned current density and total currents under MI-coupling theory are derived. We compare the derived total currents from this novel analysis of HST observations to literature values, finding good agreement in scale. These values are then compared to non-contemporaneous in-situ *Galileo* Plasma Science (PLS) measurements of the plasma flow speed and associated field-aligned current density and total current binned in the same way as the HST observations in order to perform a superposed epoch analysis. Finally, we compare the HST- and *Galileo*- derived currents directly, assuming that they fully describe the large-scale, time-averaged state of the MI-coupling system, to derive a dis-

Figure 1. Plots showing multiple views of Jupiter's northern ME on May 22, 2016 beginning at 18:02:46 UTC, as observed with HST STIS. Panel (a) shows a top-down, polar view of the northern ME, with the statistical main oval (SMO) shown with a red dashed line and λ_{III} and latitude graticules in yellow. Panel (b) shows a labeled keogram, where the observation in (a) is represented in the first (top) row. The values in both (a) and (b) are log-scaled with colors corresponding to the colorbar beneath. Panel (c) depicts the same keogram, but with a limb-brightening correction applied. Panel (d) shows the corrected keogram projected to the magnetospheric equatorial plane as a function of MLT and ρ_e, with the projected SMO corresponding to the first (dashed) and final (dotted) exposures shown in red. The values in both (c) and (d) are log-scaled, with colors corresponding to the separate colorbar beneath.

tribution of the Pedersen conductance in MLT, ρ_e, and solar CML. The resulting conductance distribution is additionally mapped back into the ionosphere. We find that the Pedersen conductance peaks in the dawn sector, and varies primarily in MLT, consistent with controlling the subcorotation of auroral forms in the dawn ME and helping resolve the tension between high degrees of field bend-back and high plasma velocities in the dawn sector.

2 Data

2.1 Hubble Space Telescope Data

Archival observations of Jupiter's ultraviolet (UV) aurorae made with the Advanced Camera for Surveys Solar Blind Channel (ACS/SBC) and Space Telescope Imaging Spectrograph (STIS) on HST were obtained for this study. These observations comprise more than 200 cumulative hours of exposure, and span 2007 and 2016−2019; this large survey is expected to be representative of the general state of Jupiter's main emission aurorae. Further details about this set of observations are presented in Rutala et al. (2022) and references therein.

Time-tagged STIS observations were split into non-overlapping 30s intervals to create images, while the typical ∼100s exposures for the ACS observations were unchanged. Images were reduced and projected onto an equirectangular planetocentric grid using the standard procedures in the Boston University HST data reduction pipeline (Clarke et al., 2009; Nichols & Cowley, 2022; Rutala et al., 2022, e.g.); the projection from the HST perspective to an equirectangular grid allows the observations to be viewed from any perspective, as illustrated by the reduced observation mapped to an orthographic polar view in Figure 1a. The factors used to convert the observed auroral brightness from counts/s to kR of unabsorbed H and H_2 emission vary with color ratio (Gustin et al., 2012), which can change rapidly on both small and large scales. Here, we estimate an effective value of the color ratio of 12 in the ME region from *Juno* ultraviolet spectrograph (UVS) based

maps of the color ratio distribution (Gérard et al., 2018). Auroral intensities in the ACS/SBC images were further multiplied by a factor of 1.4 for those using the F115LP filter and 1.6 for those using the F125LP filter, following recent changes to the SBC absolute flux calibration (Avila et al., 2019).
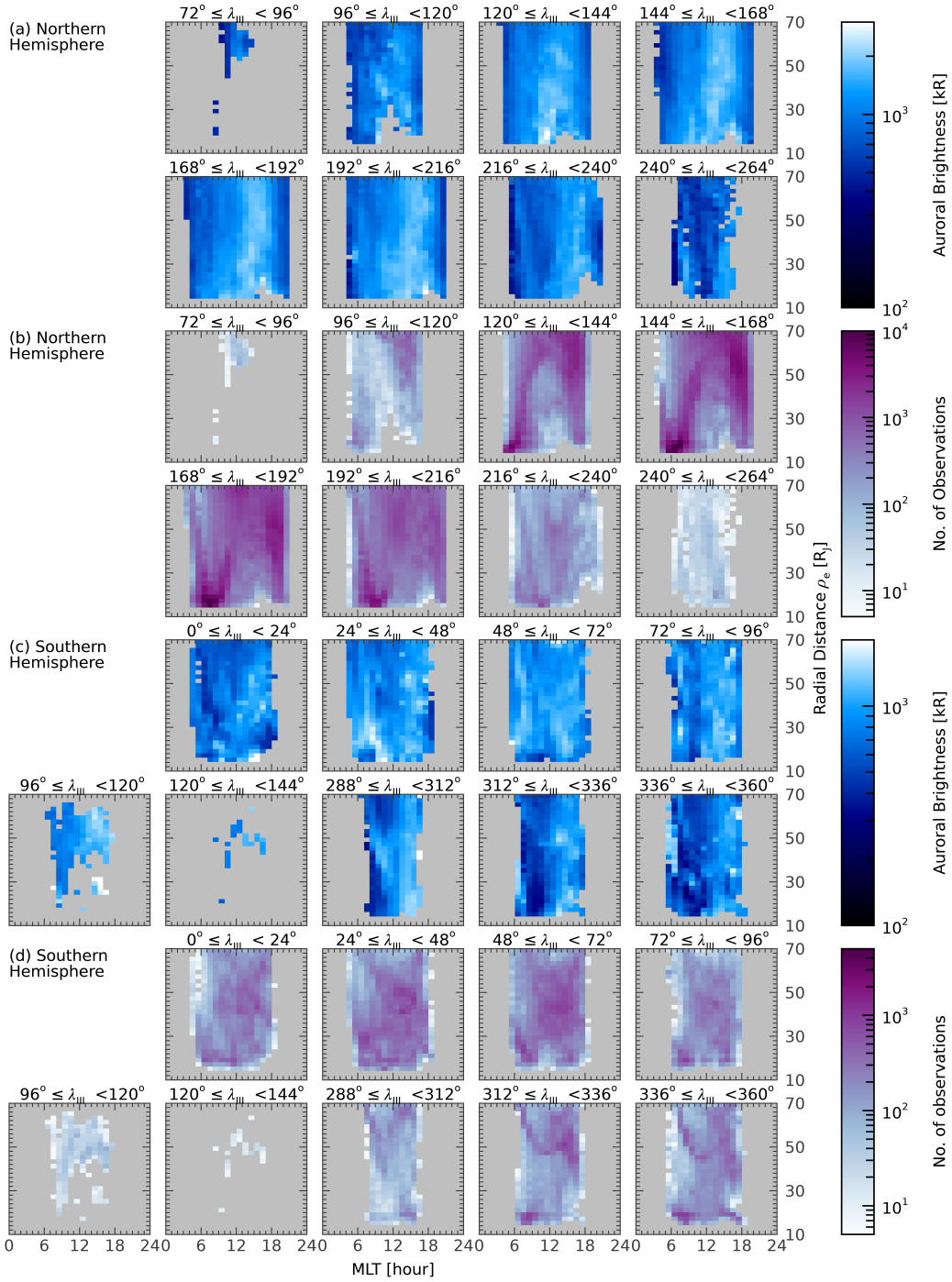
In each reduced image, an ME brightness profile is measured as the mean brightness of the brightest quartile of emission within $\pm 5°$ perpendicular to the SMO, as found by Nichols et al. (2009), in steps along the ME. 300 steps evenly spaced in distance along the SMO with dynamic sizes were found to maximize resolution while preventing overlap between pixels sampled by adjacent steps. The extracted brightness profile is stacked into a keogram for each image within the same HST visit, and aligned such that the location along the SMO is measured horizontally and exposure time is measured vertically. Figure 1b shows a keogram created in part from the observation in Figure 1a, with SIII coordinates, distance along the SMO, and MLT all labeled. Limb-brightening correction factors found as the inverse cosine of the view angle (Grodent et al., 2005) were applied to each keogram, the results of which are demonstrated in Figure 1c. The inverse-cosine correction generally overestimates the limb-brightening effect very near the edge of planet's disk as viewed by HST. The effect of this overestimation is partially countered by removing all parts of the observations within $10°$ of the limb; the slight remaining effects of the overestimation will be discussed in the Results. The keogram production process is further discussed in Rutala et al. (2022).

In each of the 288 keograms, the auroral brightness (I), local time (LT), latitude (ϕ), System III longitude (λ_{III}), and the 1σ width ($\delta\theta$) of the ME were recorded for every pixel. Pixels were then mapped from λ_{III} and ϕ in the ionosphere to magnetic local time (MLT) and radial distance in the equatorial plane of the mangetosphere (ρ_e) using the magnetic flux equivalence mapping of Vogt et al. (2011). The internal magnetic field for the mapping was specified to be the JRM09 magnetic field model (Connerney et al., 2018) which, over the spatial scales relevant here, is very similar to the more recent JRM33 model (Connerney et al., 2022). Solar CML values for the mapping were found using ephemerides from the NASA NAIF SPICE toolkit (Acton et al., 2018). The angular width of the ME, $\delta\theta$, was mapped to a radial width, $\delta\rho_e$, in the same manner. The observed and mapped parameters were then binned by 1 hour in MLT, 2 R_J in ρ_e, and 24° in solar CML; a typical, 40 minute HST observation of the Jovian aurorae spans $\sim 24^o$ of longitude as the planet rotates. Values in each bin were calculated as the arithmetic mean. Figure 1d shows the auroral brightness of the keogram in Figure 1c binned in MLT and ρ_J, with the projected SMO locations corresponding to the first and last exposures included for reference. As Figure 1d represents a ~ 40 min. observation, it effectively spans a single bin in solar CML and can as such be binned in MLT and ρ_e and displayed completely in two dimensions. Emissions mapping to radial distances less than that of SMO originate at lower latitudes than the SMO, as is the case particularly near dusk in Figure 1. The binned distributions of auroral brightness and number of observations per bin are shown in full in Figure 2; to display these distributions, which are binned in three-dimensional, each panel in Figure 2 represents the two-dimensional distribution with respect to MLT and ρ_e corresponding to a single solar CML bin.
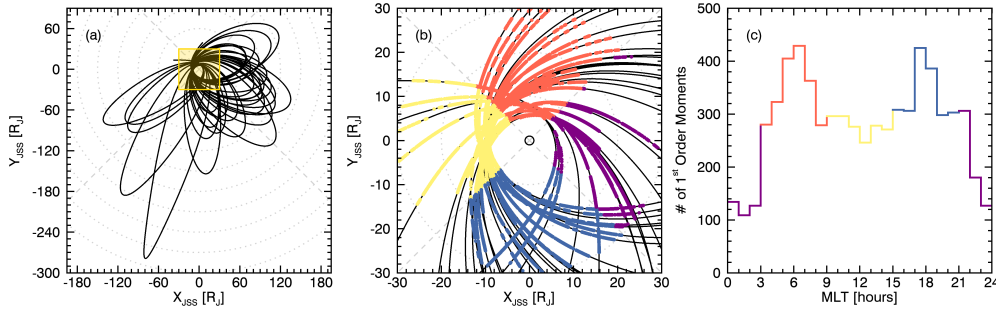
2.2 *Galileo* PLS Measurements

Plasma parameters derived from the numerical moments of *Galileo* PLS real-time science data were obtained, as calculated by Frank et al. (2023). The *Galileo* spacecraft's native Inertial Rotor Coordinate (IRC) system, a despun coordinate system based on the spacecraft's geometry, is complex (Bagenal et al., 2016) and has not been fully implemented into SPICE (Acton et al., 2018), due in part to the *Galileo* spacecraft heritage predating the SPICE toolkit. SPICE ephemerides for the *Galileo* spacecraft position are available for all 6751 moments; spacecraft pointing information is only available for 4897 of those 6751. So that the full set of moments can be used, the plasma flow

Figure 2. Two-dimensional distributions of the (a,c) auroral brightness and the (b, d) number of observations for both the (a, b) northern and the (c, d) southern hemispheres, with colors for each MLT-ρ_e bin corresponding to the colorbars to the right of each set of panels. Each distribution is labeled with the range of solar CMLs it spans; solar CML ranges for which there are no observations were excluded. In the sample analyzed here, it is evident that the northern hemisphere is typically brighter than the southern and that dusk is typically brighter than dawn.

Figure 3. Plots illustrating *Galileo* PLS coverage of the magnetosphere. Plot (a) shows all 34 *Galileo* orbits projected into Jupiter's equatorial plane in the Jupiter-Despun-Sun (JSS) reference frame, with the region spanning $\pm 30R_J$ in both dimensions highlighted in yellow. (b) A zoomed-in view of the highlighted region in (a), with individual *Galileo* PLS plasma flow speed measurements overplotted as points, colored according to MLT sector: dawn (03≤MLT<09) in orange, noon (09≤MLT<15) in yellow, dusk (15≤MLT<21) in blue, and midnight (00≤MLT<03; 21≤MLT<24) in purple. (c) A histogram of the number of *Galileo* PLS plasma flow speed measurements in each hour-wide MLT bin. The abundance of dawn and dusk observations, compared to those near noon and particularly near midnight, is evident.

251 speed is estimated as the root-sum-square of all the velocity components, as the azmi-
252 uthal component of the plasma velocity is expected to be much larger than the radial
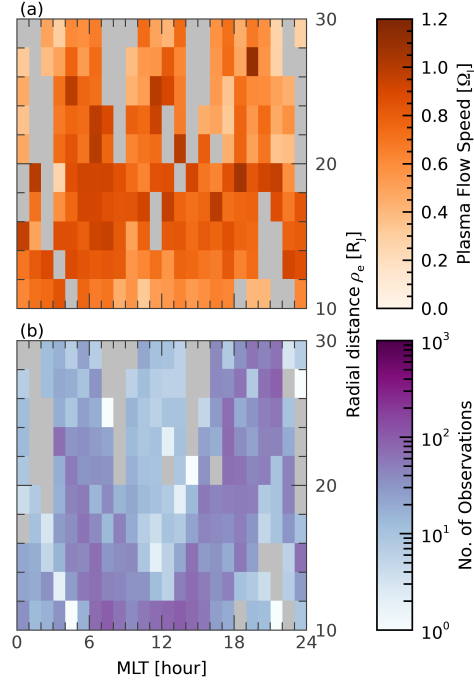253 and polar components.

254   These numerical moments span 31 of *Galileo*'s 34 orbits, and cover a combined 129
255 days. The plasma parameters span $10R_J \leq \rho_e \leq 30R_J$ within $\sim 1-2R_J$ of the equa-
256 torial plane, with larger distances from the equatorial plane corresponding to larger ra-
257 dial distances. These parameters cover all local times and SIII longitudes, with a bias
258 in local time sampling towards dawn and dusk. Figure 3 illustrates the coverage of the
259 numerical moments relative to *Galileo*'s full orbit and shows this bias. Figures 3a and
260 3b are plotted in the Jupiter-De-Spun-Sun (JSS) reference frame, which is defined to have
261 $\hat{Z}$ aligned with Jupiter's rotational axis, the Sun located in the $\hat{X}-\hat{Z}$ plane, and $\hat{Y}$ com-
262 pleting the right-hand orthogonal set. The average plasma corotation rate (R_C) was cal-
263 culated for bins spanning 1 hour in MLT and 2 R_J in ρ_e; as the middle magnetosphere
264 is dominated by magnetic local time effects rather than longitudinal effects (Vogt et al.,
265 2011; Ray et al., 2014), the *Galileo* data were not binned by the solar CML of the planet.
266 Binning of the plasma parameters was performed by averaging with weights proportional
267 to the inverse of the parameter variance to be representative of the time-averaged MI-
268 coupled system.

269   The plasma corotation rate R_C is defined as

$$R_C = \frac{v_{flow}}{\rho_e \Omega_J} = \frac{\omega_{flow}}{\Omega_J} \tag{1}$$

271 where v_{flow} is the calculated linear plasma flow velocity from the *Galileo* PLS data, ω_{flow}
272 is the angular plasma flow velocity ($\omega_{flow} = v_{flow}/\rho_e$), and Ω_J is the angular veloc-
273 ity at which Jupiter rotates (1.76×10^{-4} rad s^{-1}). R_C is averaged in each bin rather
274 than v_{flow} to account for the expected inverse relationship between equatorial distance
275 ρ_e and v_{flow}. When $v_{flow} = \rho_e \Omega_J$, the plasma is rigidly corotating with the planet and
276 $R_C = 1$. In turn, when $v_{flow} = 0$ then the plasma is fixed with respect to the Sun-

Figure 4. Two-dimensional distributions of the (a) corotation rate (R_C) of the equatorial plasma from *Galileo* PLS moments from Equation 1 and the (b) number of moments. The moments were not binned with respect to solar CML, as the middle magnetosphere is expected to vary primarily in MLT.

Jupiter geometry, or effectively fixed in MLT, and $R_C = 0$. The full set of 6751 plasma parameters used from *Galileo* PLS are summarized in Figure 4, which shows the two-dimensional distributions of the corotation rate R_C and the number of moments N with respect to MLT and ρ_e.

3 Analysis

The field-aligned current per radian of azimuth, $I_{||}$, in the coupled MI system driving Jupiter's main emission near the ionosphere can be found as

$$I_{||} = -2 \int_0^{\rho_e} j_z \rho'_e \, d\rho'_e \tag{2}$$

$$= 4\Sigma_P^* \Omega_J (1 - R_c) F_e \tag{3}$$

adapted from Equation 16 in Cowley and Bunce (2001). Here j_z is the field-aligned current density flowing out of the current sheet lying in the middle magnetosphere's equatorial region, Σ_P^* is the height-integrated effective Pedersen conductance, $\Omega_J = 1.76 \times 10^{-4}$ rad s^{-1} and R_C are the angular velocity and magnetospheric plasma corotation rates defined previously, and F_e is the equatorial flux function, a function which maps the auroral ionosphere to the equatorial middle magnetosphere along contours of constant magnetic flux. The field-aligned current per radian of azimuth $I_{||}$ can be calculated from the auroral brightness observed with HST using Equation 2 and from the plasma flow speed derived from *Galileo* PLS using Equation 3, as will be discussed in Sections 3.1 and 3.2, respectively.

3.1 Field-aligned currents from HST observations

The brightness of the ME aurorae observed with HST is directly proportional to the precipitated energy flux of auroral electrons E_f incident on the atmosphere, with a conversion factor of 10 kR per 1 mW m^{-2} (Gustin et al., 2012; Nichols & Cowley, 2022). This energy flux E_f is in turn related to the field-aligned current density just above the auroral ionosphere $j_{||}$ as

$$j_{||} = j_{||,0} \left(\pm \sqrt{2 \frac{E_f}{E_{f,0}} - 1} \right) \tag{4}$$

where $j_{||,0}$ is the maximum field-aligned current density above the ionosphere and $E_{f,0}$ is the maximum precipitated energy flux of auroral electrons, both for the case of an absence of field-aligned potentials. Equation 4 is derived by assuming the minimum necessary field-aligned potentials for currents to flow into the ionosphere. The maximum energy flux in the absence of field-aligned potentials is $E_{f,0} = 2N\sqrt{W_{th}/2\pi m_e}W_{th}$ (Equation 37 in Cowley and Bunce (2001)), which is a number flux of electrons $(2N\sqrt{W_{th}/2\pi m_e})$ multiplied by a characteristic energy (W_{th}). $E_{f,0}$ can therefore be estimated by measurable physical parameters; here, $N = 0.018$ cm^{-3} (Bagenal et al., 2016; Huscher et al., 2021) and $W_{th} = 5$ keV (Allegrini et al., 2021) are used. Similarly, the maximum field-aligned current density just above the ionosphere in the absence of field-aligned potentials is $j_{||,0} = eN\sqrt{W_{th}/2\pi m_e}$, the number flux of electrons multiplied by e, the elementary charge (Equation 28 in Cowley and Bunce (2001)).

The quantity j/B is constant along a magnetic field line provided there are no field-perpendicular currents intersecting the field line outside of the equatorial and ionospheric regions (Cowley & Bunce, 2001), so $j_{||}$ can be written as $j_z B_i/B_e$, where B_i and B_e are the strengths of the magnetic field along the field line in the ionosphere and the current sheet in the equatorial plane, respectively. The magnetic field strength in the equatorial plane of the magnetosphere B_e, is calculated from the form provided in Vogt et al. (2011), which is itself a fit to in-situ magnetic field measurements from *Pioneer 10*, *Pioneer 11*, *Voyager 1*, *Voyager 2*, *Ulysses*, and *Galileo* spanning $20 - 120$R$_J$. The magnetic field strength in the ionosphere was found using the internal magnetic field model based on *Juno*'s first 33 orbits of Connerney et al. (2022)(henceforth, JRM33), calculated to order 13 using the code provided by Wilson et al. (2023), and assuming an altitude of 1R$_J$. The magnetic field function of Vogt et al. (2011) is more appropriate for B_e than the more recent JRM33 model as it captures the significant variation of the middle and outer magnetosphere with MLT; beyond 10R$_J$, the higher order terms in the JRM33 model become negligible and the resulting field is very nearly dipolar and azimuthally symmetric.

Equation 4 can thus be substituted into Equation 2 for j_z to give

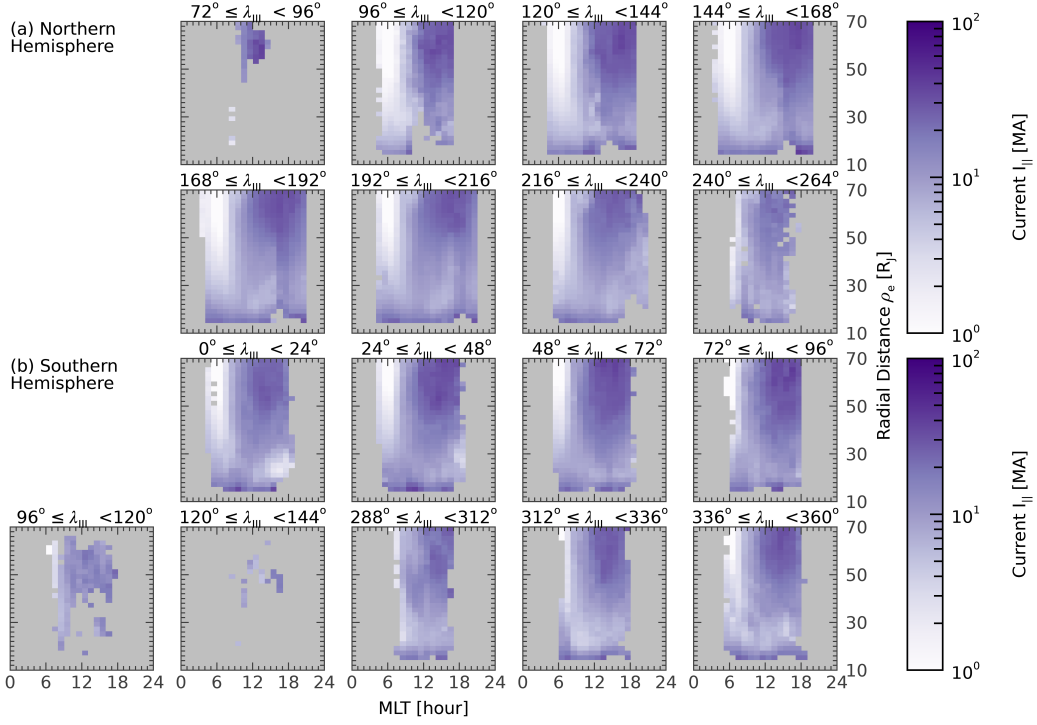$$I_{||} = -2 \int_0^{\rho_e} j_{||,0} \frac{B_e}{B_i} \left(\pm \sqrt{2 \frac{E_f}{E_{f,0}} - 1} \right) \rho_e' \, d\rho_e' \tag{5}$$
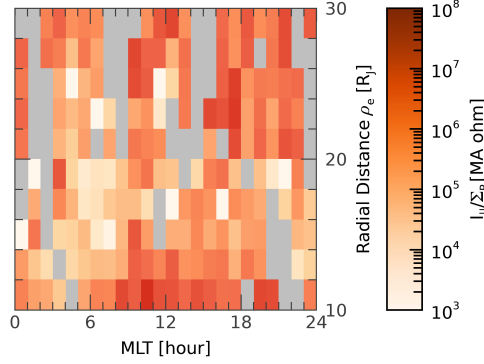
which can be used to calculate the field-aligned current per radian of azimuth $I_{||}$ corresponding to a given auroral brightness. Evaluation of Equation 5 requires and integrable auroral electron energy flux $E_f(\rho_e')$, which in turn requires a function of the auroral brightness over equatorial distance. The variation of the auroral brightness with equatorial distance illustrated in Figure 2 does not represent this function directly. Instead, these distributions show the typical values of the observed ME when the ME maps to a given location in MLT-ρ_e space, which in turn represents the maximum of the field-aligned current density j_z for a given span of solar CML. An integrable radial distribution of $E_f(\rho_e')$ is therefore approximated as a Gaussian having a peak value of E_f, a center defined by the corresponding radial bin, and a width defined by the angular width of the ME ($\delta\theta$) magnetospherically mapped to a radial width ($\delta\rho_e$). The resulting radial distributions are then numerically integrated from 0 out to the corresponding ρ_e value.

Figure 5. Two-dimensional distributions of the integrated field-aligned current per radian of azimuth ($I_{||}$ calculated from Equation 5 for the (a) northern and (b) southern hemispheres, with colors for each MLT-ρ_e bin corresponding to the colorbars to the right. Each distribution is labeled with the range of solar CMLs it covers. Generally, stronger currents are seen to occur at dusk rather than dawn, and when the magnetosphere is more perturbed (i.e., when the ME maps to more distant regions of the magnetosphere).

Figure 6.   Two-dimensional distribution of the quantity $I_{||}/\Sigma_P^*$ derived from the *Galileo* PLS moments using Equaiton 6, with colors in each MLT-ρ_e bin corresponding to the colorbar to the right. Generally, $I_{||}/\Sigma_P^*$ is seen to be smaller at dawn than at dusk.

The resulting values of $I_{||}$ we report are thus average field-aligned currents per radian of azimuth entering the ionosphere at the ME, when the location of the ME maps to the current sheet at the location specified by the corresponding bin. The distributions of $I_{||}$ with MLT, ρ_e, and solar CML in Figure 5 thus illustrate various independent MI coupling configurations rather than multiple samples of the same configuration. To clarify further, the distributions of $I_{||}$ calculated here are not expected to increase monotonically with equatorial distance ρ_e, even though the integral of $F_e(\rho_e')$ would, for the same reasons that the ME brightness does not increase monotonically with ρ_e in Figure 2.

3.2 Field-aligned currents from Galileo-PLS data

Returning to Equation 3 and rearranging, the total field-aligned current per radian of azimuth $I_{||}$ flowing into the ionosphere divided by the effective, height-integrated Pedersen conductance Σ_P^* of the ionosphere, can be found as

$$\frac{I_{||}}{\Sigma_P^*} = 4\Omega_J(1 - R_c)F_e \tag{6}$$

The height-integrated effective Pedersen conductance Σ_P^* is the sum of all conductance terms and is reduced from the true value, Σ_P, by a factor of $(1-k)$ to account for the slippage in the ion-neutral coupling in the ionosphere. The values of k range from $0 < k < 1$, with $k = 0$ corresponding to no slippage of the neutral atmosphere relative to the planet's rigid rotation rate and $k \approx 1$ corresponding to maximal slippage (Huang & Hill, 1989; Nichols & Cowley, 2003). The equatorial flux F_e, which relates locations in the ionosphere to conjugate points in the current sheet in the equatorial plane of the magnetosphere along contours of constant magnetic flux, is a function of both MLT and ρ_e and is calculated using the form provided by Ray et al. (2014). This description of $F_e(\text{MLT}, \rho_e)$ is based on a slightly modified version of the empirical magnetic field model used to map HST observations into the equatorial magnetospheric plane (Vogt et al., 2011). The differences between this and the unmodified empirical magnetic field model are greatest near the planet; the two descriptions agree throughout the middle magnetosphere where MI coupling currents flow, ensuring consistency between the values derived from *Galileo* PLS and HST observations.

The quantity $I_{||}/\Sigma_P^*$ can thus be solved for using *Galileo* PLS-derived values of the plasma corotation rate R_c and the known form of F_e. This quantity is introduced for convenience and has limited physical meaning, despite having the form of an electric po-

tential. Instead, the quantity $I_{||}/\Sigma_P^*$ groups unknown parameters together, and will allow further exploration of the distribution of Σ_P^* when compared to the values of $I_{||}$ derived from HST observations. Figure 6 shows the distributions of the quantity $I_{||}/\Sigma_P^*$ with MLT and equatorial distance ρ_e.
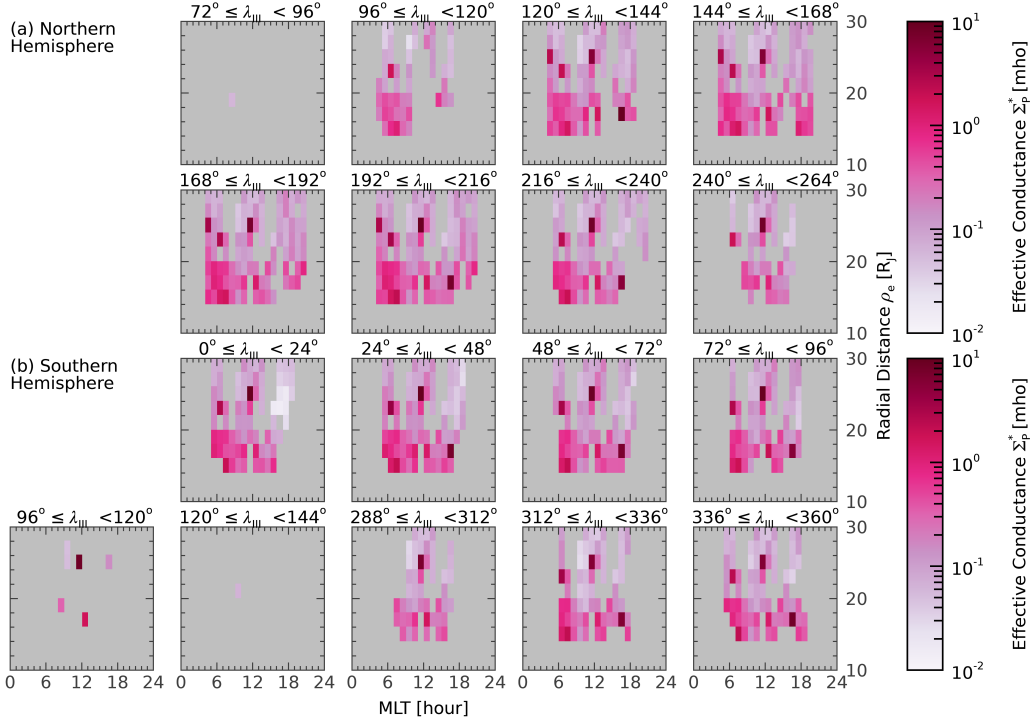
4 Results and Discussion

4.1 Azimuthally integrated field-aligned currents

First, we focus on the field-aligned current per radian azimuth $I_{||}$ derived from HST observations, which, unlike the parameter $I_{||}/\Sigma_P^*$ derived from *Galileo* measurements, is representative of the field-aligned auroral currents flowing in Jupiter's coupled MI system without any further assumptions about the ionospheric Pedersen conductance. The northern ME is found to have a median current per radian of azimuth of $I_{||} = 9.54^{+11.5}_{-6.35}$ MA rad^{-1}, while the southern ME has a median current per radian of azimuth of $I_{||} = 10.6^{+11.1}_{-6.11}$ MA rad^{-1}. These median values are found using a Monte Carlo bootstrap analysis with lognormal error perturbation (henceforth just "medians"), in order to better account for the measurement errors in the non-Gaussian distribution of currents (Curran, 2014). Upper and lower errors correspond to the 84th and 16th percentiles, respectively, to approximate 1σ errors. These median currents are in very good agreement with the currents calculated from *Juno* magnetometer measurements, both lying within the $\sim 1-27$ MA rad^{-1} range of $I_{||}$ (Nichols & Cowley, 2022) and reproducing the magnitude, after accounting for integration over azimuth, and North-South asymmetry previously measured (Kotsiaros et al., 2019).

4.2 Effective Pedersen conductance

The effective Pedersen conductance (Σ_P^*) can be calculated by dividing the field-aligned current per radian of azimuth derived from HST measurements ($I_{||}$) by the quantity derived from *Galileo* PLS moments ($I_{||}/\Sigma_P^*$). Figure 7 shows distributions of this calculated effective Pedersen conductance for the northern and southern hemispheres; these plots are limited to $10 < \rho_e \leq 30 R_J$ due to the coverage of the *Galileo* PLS moments. The binned distributions of $I_{||}/\Sigma_P^*$ are assumed to be the same at all solar CML in this analysis. We find 95% of conductances lie in the range $0.03 < \Sigma_P^* < 1.79$ mho in the north with a median of $\Sigma_P^* = 0.14^{+0.31}_{-0.08}$ mho and $0.02 < \Sigma_P^* < 2.26$ mho in the south with a median of $\Sigma_P^* = 0.14^{+0.34}_{-0.09}$ mho, with errors corresponding to the 16th and 84th percentiles. These averages are comparable to both theoretical estimates (Millward et al., 2002, 2005) and recent estimates made using *Juno* ultraviolet spectrograph (UVS) measurements and ionospheric modeling (Gérard et al., 2020, 2021) of $\Sigma_P \approx 0.5$, considering that these reported values are not reduced by the $(1 - k)$ factor. For typical values of $k \approx 0.4 - 0.7$ (Millward et al., 2005), the novel method used here to calculate the conductance of the auroral ionosphere is in good agreement with literature values.

For clarity, Figure 8 shows the same data as Figure 7, but with the medians and the $84^{th}/16^{th}$ percentile errors of the effective Pedersen conductance in each bin plotted. By comparison to the average values and errors for each hemisphere overall, the variations in conductance with respect to each binning parameter can be seen. Figures 8c and 8f show that Σ_P^* varies minimally with solar CML. Figures 8b and 8e show that the effective Pedersen conductance is generally higher at smaller radial values, corresponding to higher field-aligned currents when the magnetosphere is in a disturbed enough state for the ME to map to these distances. The conductance thus increases with current, as expected (Nichols & Cowley, 2004). The bin-to-bin variation is greatest when the conductance is interpreted as a function of MLT, as shown in Figures 8a and 8d. This significant variation in effective conductance with MLT is more likely than the variations with equatorial distance or solar CML to be related to the local time asymmetries in the appearance, distribution, and motion of ME aurorae. Both hemispheres display peaks
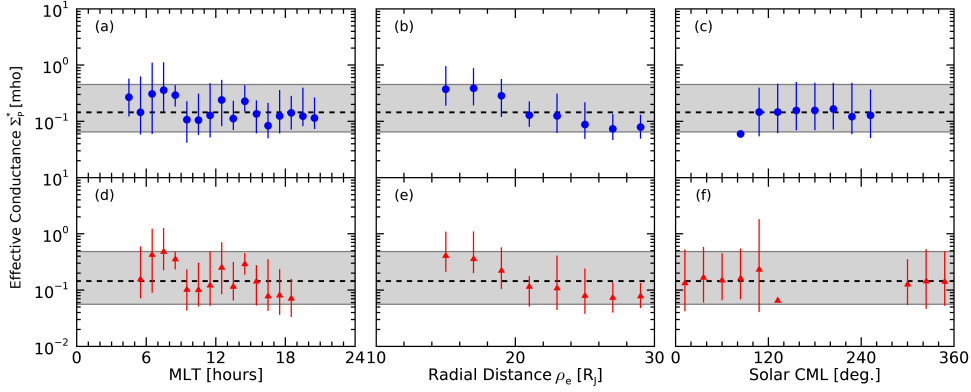
Figure 7. Two-dimensional distributions of the effective Pedersen conductance Σ_P^* for the (a) northern and (b) southern hemispheres, with the color of each MLT-ρ_e bin corresponding to the colorbars to the right. The effective Pedersen conductance is only calculated where both HST-derived and *Galileo* PLS-derived data are present. Generally, the conductance is greatest at smaller radial distances and nearer dawn.

in the effective conductance between $7-8$, $12-13$, and $14-15$ MLT. It is worth noting that, without the limb-brightening correction applied to HST-observed auroral brightness, derived field-aligned currents would be increased more near dawn and dusk than near noon, and Σ_P^* would increase proportionally. The overestimation of the limb-brightening correction factors thus results in an underestimation of the conductance near the planet's limbs at dawn and dusk, and a more accurate model of Jupiter's limb-brightening would heighten the peak in Σ_P^* between $7-8$ MLT further than the others.

Figure 9 shows the complete conductance distributions mapped onto Jupiter's auroral ionosphere for each solar CML bin, allowing the variation in Σ_P^* with local time and location relative to the SMO to be visualized. The generally increased effective Pedersen conductance near local dawn, located to the left of each frame in Figure 9, is evident. The smooth decrease in Σ_P^* with increasing ρ_e can be seen as a decrease in Σ_P^* with increasing latitude, particularly in the noon and dusk sectors, in Figure 9a. The same trend is not seen in Figure 9b, as the middle magnetosphere maps to a smaller range of latitudes in the southern ME than in the northern ME.

From the derived distributions of Σ_P^* alone, we cannot determine the cause of the variation of the conductance with MLT. It is of interest, however, that the effective Pedersen conductance peaks in the late-dawn ($7-8$ MLT) and noon ($12-13$ MLT) regions are generally colocated with known subcorotating emission features within the ME: the dawn storms and associated, less bright subcorotating emission features in the post-
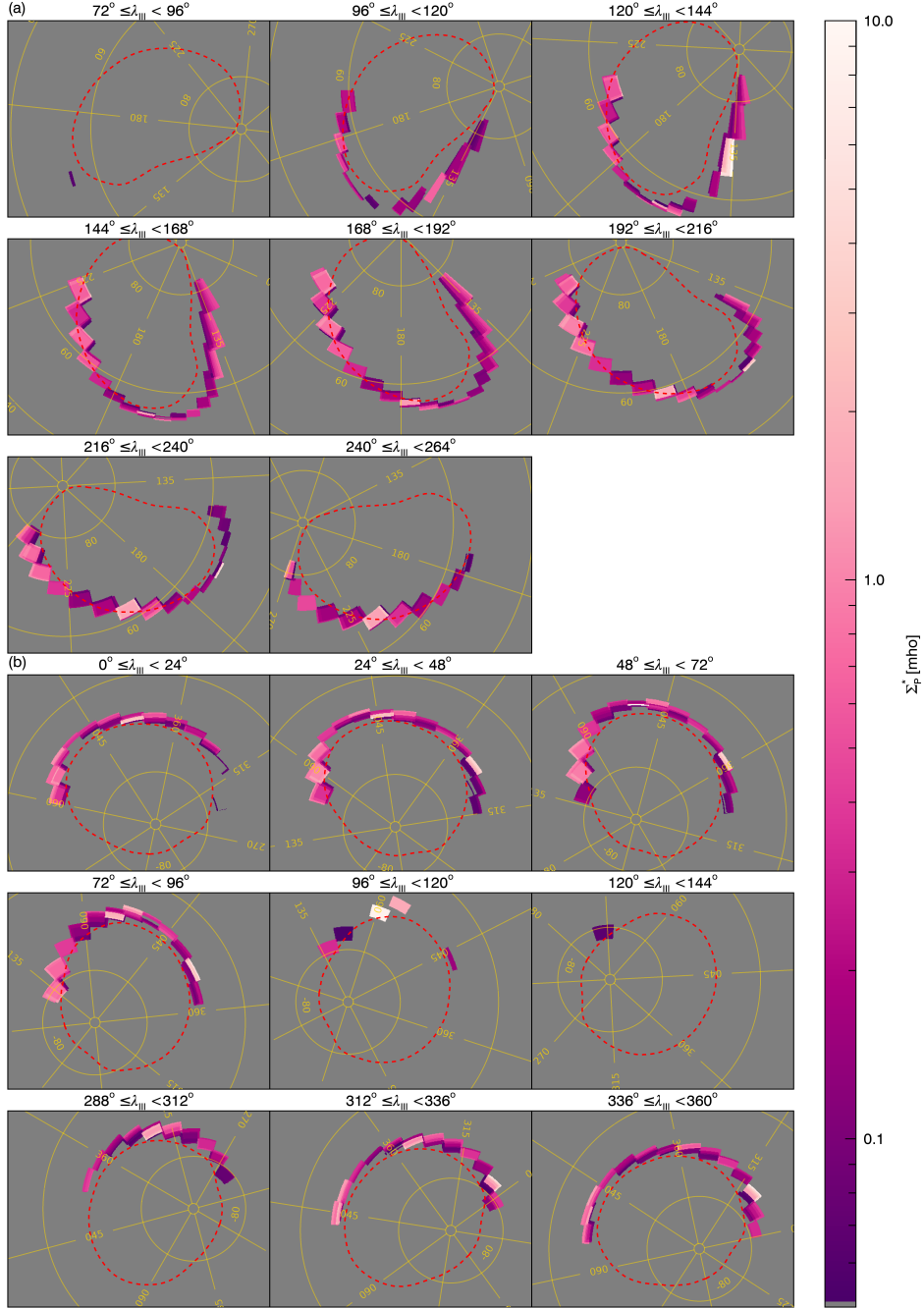
Figure 8. Plots showing the trends in the median effective Pedersen conductance Σ_P^* with MLT (a, d), ρ_e (b, e), and solar CML (c, f) for the northern (a, b, c; blue circles) and southern (d, e, f; red triangles) hemisphere ME. The conductance varies widely with MLT and insignificantly with solar CML.

dawn region (Rutala et al., 2022) and the noon discontinuity and auroral spot near noon (Radioti et al., 2008; Palmaerts et al., 2014).

The co-occurrence of increased ionospheric conductance and subcorotating auroral features within the ME was hypothesized by Rutala et al. (2022) as an explanation of subcorotational behavior near dawn. The basic premise is that, if the ionospheric conductance is locally increased for a reason unrelated to MI-coupling currents, the MI-coupling currents will increase in magnitude due to the heightened conductance, accelerating magnetospheric plasma up to the corotation rate of the planet; as the magnetosphere generally compresses from dawn through noon, the linear velocity of the recently-accelerated magnetospheric plasma would exceed the local angular corotational velocity as the system rotates, thus reducing or reversing the field-aligned currents. In the ionosphere, this would appear as a bright auroral form associated with the increased currents which ends abruptly as the currents reverse, thus appearing fixed in local time. This picture meshes well with the noon ME discontinuity observed by Radioti et al. (2008), which is expected to be associated with reduced or reversed field-aligned currents. The secondary peak in Σ_P^* near noon may be associated with the subcorotational noon auroral spot (Palmaerts et al., 2014), as following noon the magnetosphere expands again, thus requiring increased field-aligned currents to bring plasma up to local corotational velocity.

This second peak in Σ_P^* near 12 MLT may instead be caused by increased field-aligned currents caused by shearing motions of magnetospheric plasma, as modeled by Chané et al. (2018). Generally, as an increase in the field-aligned currents will cause an increase in the effective Pedersen conductance, we cannot distinguish between cause and effect with this data set: high currents could cause increased conductance, or heightened conductance may drive increased currents. It is of note that the conductance distributions found in Figure 8 are more similar to the modeled conductance distribution in LT found by Tao et al. (2010) than to the distributions in solar CML found by Gérard et al. (2020, 2021). In the latter case, the differences may in part be explained by the difference in observational integration time. Images from HST span non-overlapping $30-100$ s exposures while spectral images from *Juno* were integrated over $20-50$ min (Gérard et al., 2020, 2021), which would introduce more smoothing into the *Juno* UVS based maps than is present in this analysis. The similarity in form between the Σ_P^* distributions found here and those of Tao et al. (2010) may indicate a relationship between heightened dawn

Figure 9. Polar, orthographic views of Jupiter's north auroral region, with the derived Σ_P^* distributions shown mapped onto the planet by mapping MLT and ρ_e onto λ_{III} and ϕ. Each frame corresponds to one solar CML bin with the mean solar CML, and hence noon local time, located at the bottom of the image. The SMO is shown by a red-dashed line, and λ_{III} and ϕ graticules are shown in yellow. Values of Σ_P^* have been log-scaled and correspond to the colorbar to the right. The increased conductance near dawn, toward the left side of each frame, can be seen, as can the increased conductance at lower latitudes (mapping to smaller ρ_e).

sector conductance and incident solar extreme ultraviolet (EUV) photons, which increase the Pedersen conductance by ionizing the ionosphere.

5 Conclusions

We have outlined a novel method for deriving values of the effective Pedersen conductance Σ_P^* of Jupiter's ME auroral ionosphere by combining remote observations of the Jovian ME and in-situ observations of the angular velocity, or corotation rate, of middle magnetospheric plasma. This method has been developed from the theoretical understanding of MI coupling at Jupiter, which links the field-aligned currents entering the ionosphere, estimated from the auroral brightness measured with HST, to the motion of middle magnetospheric plasma, calculated by moment analysis of *Galileo* PLS measurements. Equivalent regions of the auroral ionosphere and equatorial magnetosphere are found using magnetic flux equivalence mapping. The non-overlapping 288 HST observations and 6751 *Galileo* measurements used in this analysis are taken to be representative of the time-averaged Jupiter system.

From the HST observations, we find field-aligned currents entering the ionosphere of $I_{||} = 9.54_{-6.35}^{+11.5}$ MA rad^{-1} and $I_{||} = 10.6_{-6.11}^{+11.1}$ MA rad^{-1}, corresponding to the northern and southern ME, respectively, in agreement with recent *Juno*-based measurements (Kotsiaros et al., 2019; Nichols & Cowley, 2022) and theoretical estimates (Hill, 2001; Cowley & Bunce, 2001). Combining these values with the parameter $I_{||}/\Sigma_P^*$ derived from in-situ *Galileo* PLS measurements, we find the effective Pedersen conductance Σ_P^*, reduced from the true Pedersen conductance by a factor of $1 - k \approx 0.5$. Σ_P^* ranges between $0.03 < \Sigma_P^* < 1.79$ mho in the north and $0.02 < \Sigma_P^* < 2.26$ mho in the south, with typical values of $\Sigma_P^* = 0.14_{-0.08}^{+0.31}$ mho and $\Sigma_P^* = 0.14_{-0.09}^{+0.34}$ mho in the northern and southern ME, respectively. These typical values are consistent with theoretical and modeled values (Millward et al., 2002, 2005; Gérard et al., 2020, 2021), but the distributions of Σ_P^* we find reveal that it varies primarily in MLT, rather than solar CML. This analysis indicates that the field-aligned currents derived from MI coupling theory, which have historically been used to explain Jupiter's ME, adequately describe the relationship between ME auroral brightness and the motion of middle magnetospheric plasma. Further, the heightened effective Pedersen conductance near MLTs of $07-08$ and $12-13$ MLT we find are approximately co-located with auroral features in the ME with subcorotational motions (Rutala et al., 2022; Radioti et al., 2008; Palmaerts et al., 2014). The results we present are compatible with the theory that solar EUV ionization of the auroral ionosphere is key to controlling the motions of subcorotational auroral features in the dawn sector. We cannot, however, distinguish between this case and the case of otherwise-increased dawn currents causing locally elevated conductances. Breaking the observational degeneracy between these cases should be done with comparisons of the distributions found here to models of the field-aligned currents flowing in the MI coupling system under varying ionospheric conductance conditions.

Open Research

All Hubble Space Telescope observations used in this analysis are available at the Mikulski Archive for Space Telescopes hosted by the Space Telescope Science Institute, and have been collected into a single dataset for ease of access (Rutala, 2022). All *Galileo* PLS real-time-science data are available through the Planetary Plasma Interaction (PPI) node of the Planetary Data System (PDS) (Frank et al., 2023). This research made use of the ionosphere-magnetosphere mapping code of Vogt et al. (2011) and the internal magnetic field model of Connerney et al. (2022) as made available by Wilson et al. (2023) to allow comparison between in-situ and remote measurements.

Acknowledgments

References

Acton, C., Bachman, N., Semenov, B., & Wright, E. (2018, January). A look towards the future in the handling of space science mission geometry. *Planetary and Space Science*, *150*, 9–12. doi: 10.1016/j.pss.2017.02.013

Allegrini, F., Kurth, W. S., Elliott, S. S., Saur, J., Livadiotis, G., Nicolaou, G., . . . Wilson, R. J. (2021). Electron Partial Density and Temperature Over Jupiter's Main Auroral Emission Using Juno Observations. *Journal of Geophysical Research: Space Physics*, *126*(9), e2021JA029426. doi: 10.1029/2021JA029426

Avila, R. J., Bohlin, R., Hathi, N., Lockwood, S., Lim, P. L., & De La Peña, M. (2019, October). *SBC Absolute Flux Calibration* (Tech. Rep.). Space Telescope Science Institute.

Bagenal, F., Wilson, R. J., Siler, S., Paterson, W. R., & Kurth, W. S. (2016, May). Survey of Galileo plasma observations in Jupiter's plasma sheet. *Journal of Geophysical Research: Planets*, *121*(5), 871–894. doi: 10.1002/2016JE005009

Bonfond, B., Gladstone, G. R., Grodent, D., Greathouse, T. K., Versteeg, M. H., Hue, V., . . . Kurth, W. S. (2017, May). Morphology of the UV aurorae Jupiter during Juno's first perijove observations. *Geophysical Research Letters*, *44*(10), 4463–4471. doi: 10.1002/2017GL073114

Bonfond, B., Gustin, J., Gérard, J. C., Grodent, D., Radioti, A., Palmaerts, B., . . . Tao, C. (2015, October). The far-ultraviolet main auroral emission at Jupiter - Part 1: Dawn-dusk brightness asymmetries. *Annales Geophysicae*, *33*(10), 1203–1209. doi: 10.5194/angeo-33-1203-2015

Bonfond, B., Yao, Z., & Grodent, D. (2020, November). Six Pieces of Evidence Against the Corotation Enforcement Theory to Explain the Main Aurora at Jupiter. *Journal of Geophysical Research: Space Physics*, *125*(11), e28152. doi: 10.1029/2020JA028152

Bonfond, B., Yao, Z. H., Gladstone, G. R., Grodent, D., Gérard, J. C., Matar, J., . . . Bolton, S. J. (2021, March). Are Dawn Storms Jupiter's Auroral Substorms? *AGU Advances*, *2*(1), e00275. doi: 10.1029/2020AV000275

Caldwell, J., Turgeon, B., & Hua, X. M. (1992, September). Hubble space telescope imaging of the north polar aurora on jupiter. *Science*, *257*(5076), 1512–1515. doi: 10.1126/science.257.5076.1512

Chané, E., Palmaerts, B., & Radioti, A. (2018, September). Periodic shearing motions in the Jovian magnetosphere causing a localized peak in the main auroral emission close to noon. *Planetary and Space Science*, *158*, 110–117. doi: 10.1016/j.pss.2018.04.023

Clarke, J. T., Grodent, D., Cowley, S. W. H., Bunce, E. J., Zarka, P., Connerney, J. E. P., & Satoh, T. (2004). Jupiter's aurora. In F. Bagenal, T. E. Dowling, & W. B. McKinnon (Eds.), *Jupiter. The Planet, Satellites and Magnetosphere* (Vol. 1, pp. 639–670).

Clarke, J. T., Nichols, J., Gérard, J.-C., Grodent, D., Hansen, K. C., Kurth, W., . . . Cecconi, B. (2009). Response of Jupiter's and Saturn's auroral activity to the solar wind. *Journal of Geophysical Research: Space Physics*, *114*(A5). doi: 10.1029/2008JA013694

Connerney, J. E. P., Kotsiaros, S., Oliversen, R. J., Espley, J. R., Joergensen, J. L., Joergensen, P. S., . . . Levin, S. M. (2018). A New Model of Jupiter's Magnetic Field From Juno's First Nine Orbits. *Geophysical Research Letters*, *45*(6), 2590–2596. doi: 10.1002/2018GL077312

Connerney, J. E. P., Timmins, S., Oliversen, R. J., Espley, J. R., Joergensen, J. L., Kotsiaros, S., . . . Levin, S. M. (2022, February). A New Model of Jupiter's Magnetic Field at the Completion of Juno's Prime Mission. *Journal of Geophysical Research: Planets*, *127*(2), e07055. doi: 10.1029/2021JE007055

Cowley, S. W. H., & Bunce, E. J. (2001). Origin of the main auroral oval in Jupiter's coupled magnetosphere–ionosphere system. *Planetary and Space Science*, *49*(10), 1067–1088. doi: 10.1016/S0032-0633(00)00167-7

Curran, P. A. (2014, November). Monte Carlo error analyses of Spearman's rank test. *arXiv e-prints*, arXiv:1411.3816.

Frank, L., Paterson, W., & Ackerson, K. (2023). *Galileo plasma science instrument jupiter rts moments derived bundle* [dataset]. NASA Planetary Data System. Retrieved from https://pds-ppi.igpp.ucla.edu/search/view/?id=pds://PPI/galileo-pls-jup-derived doi: doi.org/10.17189/jbaw-bm37

Gérard, J.-C., Dols, V., Prangé, R., & Paresce, F. (1994). The morphology of the north Jovian ultraviolet aurora observed with the Hubble Space Telescope. *Planetary and Space Science*, *42*(11), 905–917. doi: 10.1016/0032-0633(94)90051-5

Gérard, J.-C., Gkouvelis, L., Bonfond, B., Grodent, D., Gladstone, G. R., Hue, V., . . . Blanc, M. (2020). Spatial Distribution of the Pedersen Conductance in the Jovian Aurora From Juno-UVS Spectral Images. *Journal of Geophysical Research: Space Physics*, *125*(8), e2020JA028142. doi: 10.1029/2020JA028142

Gérard, J.-C., Gkouvelis, L., Bonfond, B., Grodent, D., Gladstone, G. R., Hue, V., . . . Giles, R. S. (2021). Variability and Hemispheric Symmetry of the Pedersen Conductance in the Jovian Aurora. *Journal of Geophysical Research: Space Physics*, *126*(4), e2020JA028949. doi: 10.1029/2020JA028949

Gérard, J. C., Grodent, D., Prange, R., Waite, J. H., Gladstone, G. R., Dols, V., . . . Franke, K. A. (1994, December). A Remarkable Auroral Event on Jupiter Observed in the Ultraviolet with the Hubble Space Telescope. *Science*, *266*(5191), 1675–1678. doi: 10.1126/science.266.5191.1675

Gérard, J.-C., Grodent, D., Radioti, A., Bonfond, B., & Clarke, J. T. (2013). Hubble observations of Jupiter's north–south conjugate ultraviolet aurora. *Icarus*, *226*(2), 1559–1567. doi: 10.1016/j.icarus.2013.08.017

Gérard, J. C., Mura, A., Bonfond, B., Gladstone, G. R., Adriani, A., Hue, V., . . . Levin, S. M. (2018, September). Concurrent ultraviolet and infrared observations of the north Jovian aurora during Juno's first perijove. *Icarus*, *312*, 145–156. doi: 10.1016/j.icarus.2018.04.020

Greathouse, T., Gladstone, R., Versteeg, M., Hue, V., Kammer, J., Giles, R., . . . Vogt, M. F. (2021, December). Local Time Dependence of Jupiter's Polar Auroral Emissions Observed by Juno UVS. *Journal of Geophysical Research:*

Planets, *126*(12), e06954. doi: 10.1029/2021JE006954

Grodent, D., Bonfond, B., Gérard, J.-C., Radioti, A., Gustin, J., Clarke, J. T., ... Connerney, J. E. P. (2008, September). Auroral evidence of a localized magnetic anomaly in Jupiter's northern hemisphere. *Journal of Geophysical Research: Space Physics*, *113*(A9), A09201. doi: 10.1029/2008JA013185

Grodent, D., Clarke, J. T., Kim, J., Waite, J. H., & Cowley, S. W. H. (2003, November). Jupiter's main auroral oval observed with HST-STIS. *Journal of Geophysical Research: Space Physics*, *108*(A11), 1389. doi: 10.1029/2003JA009921

Grodent, D., Gérard, J.-C., Cowley, S. W. H., Bunce, E. J., & Clarke, J. T. (2005). Variable morphology of Saturn's southern ultraviolet aurora. *Journal of Geophysical Research: Space Physics*, *110*(A7). doi: 10.1029/2004JA010983

Gustin, J., Bonfond, B., Grodent, D., & Gérard, J.-C. (2012). Conversion from HST ACS and STIS auroral counts into brightness, precipitated power, and radiated power for H2 giant planets. *Journal of Geophysical Research: Space Physics*, *117*(A7). doi: 10.1029/2012JA017607

Hill, T. W. (1979, November). Inertial limit on corotation. *Journal of Geophysical Research: Space Physics*, *84*(A11), 6554–6558. doi: 10.1029/JA084iA11p06554

Hill, T. W. (2001). The Jovian auroral oval. *Journal of Geophysical Research: Space Physics*, *106*(A5), 8101–8107. doi: 10.1029/2000JA000302

Huang, T. S., & Hill, T. W. (1989, April). Corotation lag of the Jovian atmosphere, ionosphere, and magnetosphere. *Journal of Geophysical Research: Space Physics*, *94*(A4), 3761–3765. doi: 10.1029/JA094iA04p03761

Huscher, E., Bagenal, F., Wilson, R. J., Allegrini, F., Ebert, R. W., Valek, P. W., ... Levin, S. M. (2021). Survey of Juno Observations in Jupiter's Plasma Disk: Density. *Journal of Geophysical Research: Space Physics*, *126*(8), e2021JA029446. doi: 10.1029/2021JA029446

Khurana, K. K., & Schwarzl, H. K. (2005, July). Global structure of Jupiter's magnetospheric current sheet. *Journal of Geophysical Research: Space Physics*, *110*(A7), A07227. doi: 10.1029/2004JA010757

Kita, H., Kimura, T., Tao, C., Tsuchiya, F., Murakami, G., Yamazaki, A., ... Fujimoto, M. (2019, December). Jovian UV Aurora's Response to the Solar Wind: Hisaki EXCEED and Juno Observations. *Journal of Geophysical Research: Space Physics*, *124*(12), 10,209–10,218. doi: 10.1029/2019JA026997

Kotsiaros, S., Connerney, J. E. P., Clark, G., Allegrini, F., Gladstone, G. R., Kurth, W. S., ... Levin, S. M. (2019, July). Birkeland currents in Jupiter's magnetosphere observed by the polar-orbiting Juno spacecraft. *Nature Astronomy*, *3*, 904–909. doi: 10.1038/s41550-019-0819-7

Krupp, N., Lagg, A., Livi, S., Wilken, B., Woch, J., Roelof, E. C., & Williams, D. J. (2001, November). Global flows of energetic ions in Jupiter's equatorial plane: First-order approximation. *Journal of Geophysical Research: Space Physics*, *106*(A11), 26017–26032. doi: 10.1029/2000JA900138

Mauk, B. H., Clark, G., Gladstone, G. R., Kotsiaros, S., Adriani, A., Allegrini, F., ... Rymer, A. M. (2020, March). Energetic Particles and Acceleration Regions Over Jupiter's Polar Cap and Main Aurora: A Broad Overview. *Journal of Geophysical Research: Space Physics*, *125*(3), e27699. doi: 10.1029/2019JA027699

Mauk, B. H., Haggerty, D. K., Paranicas, C., Clark, G., Kollmann, P., Rymer, A. M., ... Valek, P. (2017, September). Discrete and broadband electron acceleration in Jupiter's powerful aurora. *Nature*, *549*(7670), 66–69. doi: 10.1038/nature23648

Mauk, B. H., Haggerty, D. K., Paranicas, C., Clark, G., Kollmann, P., Rymer, A. M., ... Valek, P. (2018, February). Diverse Electron and Ion Acceleration Characteristics Observed Over Jupiter's Main Aurora. *Geophysical Research*

Letters, *45*(3), 1277–1285. doi: 10.1002/2017GL076901

Millward, G., Miller, S., Stallard, T., Achilleos, N., & Aylward, A. D.   (2005, January).   On the dynamics of the jovian ionosphere and thermosphere.. IV. Ion-neutral coupling. *Icarus*, *173*(1), 200–211. doi: 10.1016/j.icarus.2004.07.027

Millward, G., Miller, S., Stallard, T., Aylward, A. D., & Achilleos, N.   (2002).   On the Dynamics of the Jovian Ionosphere and Thermosphere: III. The Modelling of Auroral Conductivity. *Icarus*, *160*(1), 95–107. doi: 10.1006/icar.2002.6951

Nichols, J. D., Allegrini, F., Bagenal, F., Bunce, E. J., Cowley, S. W. H., Ebert, R. W., . . . Yao, Z.   (2020, August).   An Enhancement of Jupiter's Main Auroral Emission and Magnetospheric Currents.   *Journal of Geophysical Research: Space Physics*, *125*(8), e27904. doi: 10.1029/2020JA027904

Nichols, J. D., Badman, S. V., Bagenal, F., Bolton, S. J., Bonfond, B., Bunce, E. J., . . . Yoshikawa, I.   (2017, August).   Response of Jupiter's auroras to conditions in the interplanetary medium as measured by the Hubble Space Telescope and Juno.   *Geophysical Research Letters*, *44*(15), 7643–7652.   doi: 10.1002/2017GL073029

Nichols, J. D., Clarke, J. T., Gérard, J. C., Grodent, D., & Hansen, K. C.   (2009, June).   Variation of different components of Jupiter's auroral emission. *Journal of Geophysical Research: Space Physics*, *114*(A6), A06210.   doi: 10.1029/2009JA014051

Nichols, J. D., & Cowley, S.   (2004, May).   Magnetosphere-ionosphere coupling currents in Jupiter's middle magnetosphere: Effect of precipitation-induced enhancement of the ionospheric Pedersen conductivity.   *Annales Geophysicae*, *22*(5), 1799–1827. doi: 10.5194/angeo-22-1799-2004

Nichols, J. D., & Cowley, S. W. H. (2003, July). Magnetosphere-ionosphere coupling currents in Jupiter's middle magnetosphere: Dependence on the effective ionospheric Pedersen conductivity and iogenic plasma mass outflow rate.   *Annales Geophysicae*, *21*(7), 1419–1441. doi: 10.5194/angeo-21-1419-2003

Nichols, J. D., & Cowley, S. W. H.   (2005, March).   Magnetosphere-ionosphere coupling currents in Jupiter's middle magnetosphere: Effect of magnetosphere-ionosphere decoupling by field-aligned auroral voltages.   *Annales Geophysicae*, *23*(3), 799–808. doi: 10.5194/angeo-23-799-2005

Nichols, J. D., & Cowley, S. W. H.   (2022).   Relation of Jupiter's Dawnside Main Emission Intensity to Magnetospheric Currents During the Juno Mission. *Journal of Geophysical Research: Space Physics*, *127*(1), e2021JA030040.   doi: 10.1029/2021JA030040

Palmaerts, B., Radioti, A., Grodent, D., Chané, E., & Bonfond, B.   (2014).   Transient small-scale structure in the main auroral emission at Jupiter.   *Journal of Geophysical Research: Space Physics*, *119*(12), 9931–9938.   doi: 10.1002/2014JA020688

Radioti, A., Gérard, J.-C., Grodent, D., Bonfond, B., Krupp, N., & Woch, J. (2008).   Discontinuity in Jupiter's main auroral oval.   *Journal of Geophysical Research: Space Physics*, *113*(A1). doi: 10.1029/2007JA012610

Ray, L. C., Achilleos, N. A., Vogt, M. F., & Yates, J. N.   (2014).   Local time variations in Jupiter's magnetosphere-ionosphere coupling system.   *Journal of Geophysical Research: Space Physics*, *119*(6), 4740–4751.   doi: 10.1002/2014JA019941

Ray, L. C., Ergun, R. E., Delamere, P. A., & Bagenal, F.   (2010).   Magnetosphere-ionosphere coupling at Jupiter: Effect of field-aligned potentials on angular momentum transport.   *Journal of Geophysical Research: Space Physics*, *115*(A9). doi: 10.1029/2010JA015423

Rutala, M. J. (2022). *Data for rutala et al. 2022* [dataset]. MAST. Retrieved from https://archive.stsci.edu/doi/resolve/resolve.html?doi=10.17909/ekt0-mf55 doi: doi:10.17909/ekt0-mf55

Rutala, M. J., Clarke, J. T., Mullins, J. D., & Nichols, J. D. (2022, June). Illuminat-

ing the Motions of Jupiter's Auroral Dawn Storms. *Journal of Geophysical Research: Space Physics*, *127*(6), e30448. doi: 10.1029/2022JA030448

Smith, C. G. A., & Aylward, A. D. (2009, January). Coupled rotational dynamics of Jupiter's thermosphere and magnetosphere. *Annales Geophysicae*, *27*(1), 199–230. doi: 10.5194/angeo-27-199-2009

Southwood, D. J., & Kivelson, M. G. (2001). A new perspective concerning the influence of the solar wind on the Jovian magnetosphere. *Journal of Geophysical Research: Space Physics*, *106*(A4), 6123–6130. doi: 10.1029/2000JA000236

Tao, C., Fujiwara, H., & Kasaba, Y. (2009, August). Neutral wind control of the Jovian magnetosphere-ionosphere current system. *Journal of Geophysical Research: Space Physics*, *114*(A8), A08307. doi: 10.1029/2008JA013966

Tao, C., Fujiwara, H., & Kasaba, Y. (2010). Jovian magnetosphere–ionosphere current system characterized by diurnal variation of ionospheric conductance. *Planetary and Space Science*, *58*(3), 351–364. doi: 10.1016/j.pss.2009.10.005

Vogt, M. F., Kivelson, M. G., Khurana, K. K., Walker, R. J., Bonfond, B., Grodent, D., & Radioti, A. (2011). Improved mapping of Jupiter's auroral features to magnetospheric sources. *Journal of Geophysical Research: Space Physics*, *116*(A3). doi: 10.1029/2010JA016148

Walker, R. J., & Ogino, T. (2003, April). A simulation study of currents in the Jovian magnetosphere. *Planetary and Space Science*, *51*(4-5), 295–307. doi: 10.1016/S0032-0633(03)00018-7

Wilson, R. J., Vogt, M. F., Provan, G., Kamran, A., James, M. K., Brennan, M., & Cowley, S. W. H. (2023, February). Internal and external jovian magnetic fields: Community code to serve the magnetospheres of the outer planets community. , *219*(15), 15. doi: 10.1007/s11214-023-00961-3